

Reprinted from

MATERIALS SCIENCE AND TECHNOLOGY

The Institute of Materials

Textures of ferritic stainless steels

D. Raabe and K. Lücke

Whereas much research has been carried out on the texture development of Fe-Si steels or low carbon steels, very little attention has been given to the texture formation and investigation of the underlying mechanisms in Fe-Cr steels. Ferritic stainless steels containing between 11 and 17%Cr establish an important group of alloys owing to their good mechanical behaviour and corrosion resistance. Various industrial problems, such as roping or optimisation of deep drawability, can be tackled by means of quantitative texture analysis. Therefore, fundamental aspects concerning the inhomogeneity of the hot and cold rolled band, the origin of Goss texture after annealing, and selective particle drag during recrystallisation of alloys with finely dispersed Nb and Ti carbonitrides have been discussed.

© 1993 The Institute of Materials. Manuscript received 27 April 1992; in final form 21 August 1992. The authors are at the Institut für Metallkunde und Metallphysik, RWTH Aachen, Aachen, Germany.

Introduction

Ferritic high grade steels containing 11–17%Cr establish an important group of construction materials owing to their good mechanical properties and corrosion resistance. Several problems in the industrial processing of these steels derive from the texture. For example, the phenomenon of roping during cold rolling of Fe–17Cr, which leads to poor surface quality, appears to result from topological aspects of the texture. The inhomogeneity through the thickness of the cold rolled and recrystallised steel is due to the inherited texture profile of the hot rolled band. During recrystallisation of microalloyed Fe–Cr steels, deviations from the desired texture with a $\langle 111 \rangle$ fibre parallel normal direction, leads to a decrease of the Lankford value and hence of deep drawability.

As a result of these technological problems, a thorough survey of the texture development and the underlying

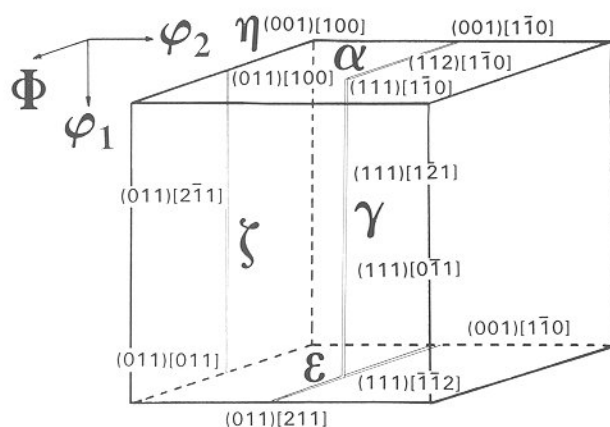
mechanisms in Fe–Cr alloys was deemed to be urgently required. For this purpose, quantitative texture analysis and metallography have been applied to investigate various industrial Fe–Cr alloys with respect to hot rolling, cold rolling, and recrystallisation.

Experimental

Five ferritic high grade steels containing between 11 and 17%Cr have been analysed. To investigate the influence of stable particles, four of the steels were microalloyed with Nb or Ti (see Table 1). All steels were industrially hot rolled to a thickness of 3 mm, starting between 1100 and 1150°C in the first pass and finishing in the temperature range 920–970°C. After hot rolling, the steels were annealed at 1000°C. Cold deformation was carried out on a laboratory rolling mill to $\varepsilon = 40, 50, 60, 70, 80$, and 90%, rotating the sample 180° about its normal and rolling directions after each pass. Since homogeneous deformation is primarily determined by the ratio of contact length l_d to sheet thickness d , a ratio of $1 < l_d < 3$ was obtained during cold rolling. After cold rolling, the samples were annealed for 5 min at 850 or 950°C in a salt bath.

All textures were quantitatively examined by measuring the four incomplete pole figures $\{110\}$, $\{200\}$, $\{112\}$, and $\{103\}$ from an area of 14.24 mm^2 in the range of the pole distance angle α from 5° to 85° with $\text{Mo K}\alpha_1$ radiation in the backreflection mode.¹ Since the interpretation of pole figures taken from polycrystals is ambiguous because of the superposition of the types of pole considered, the orientation distribution function (ODF) was calculated by the series expansion method ($l_{\text{max}} = 22$).² In the case of cubic-orthorhombic symmetry, an orientation can then be presented by the three Euler angles in the reduced Euler space.

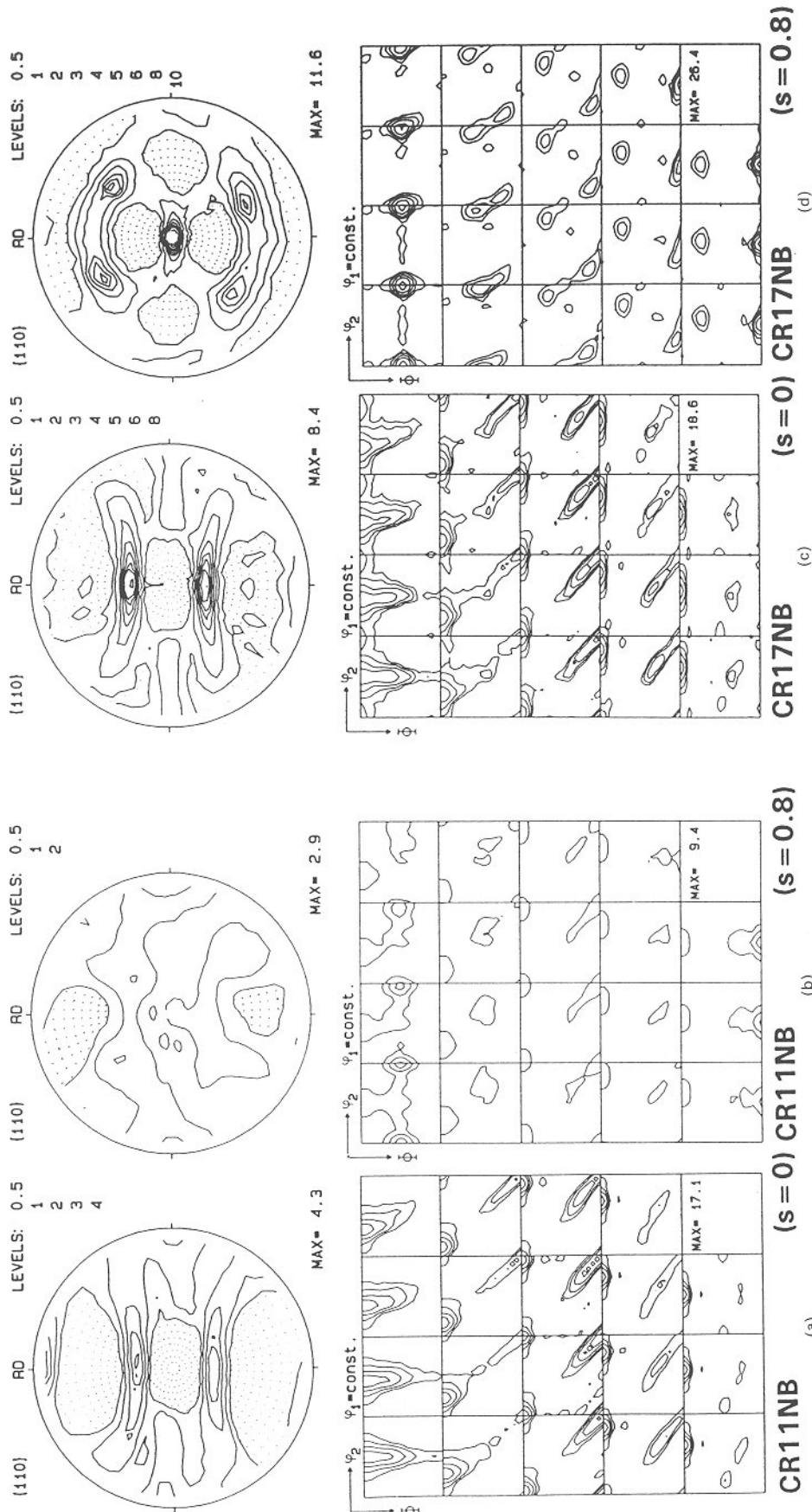
Bcc metals tend to develop strong fibre textures,³⁻⁵ so it is often convenient to represent the textures by iso-intensity diagrams in φ_1 sections or by fibre diagrams^{6,7} (see Fig. 1).



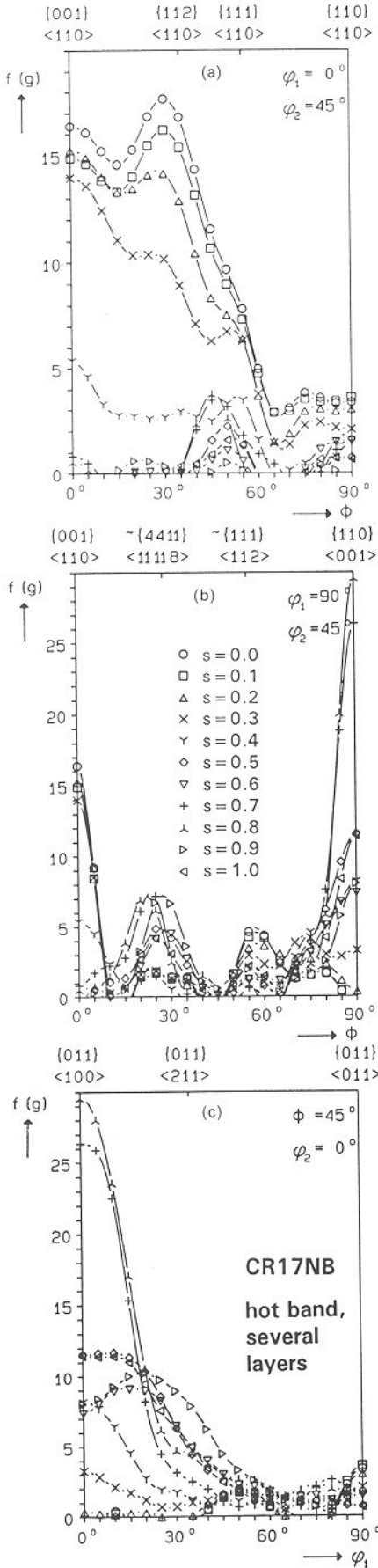
α fibre
 $\langle 110 \rangle \parallel$ RD with $\{001\}\langle 110 \rangle - \{112\}\langle 110 \rangle$ and $\{111\}\langle 110 \rangle$
 γ fibre
 $\{111\} \parallel$ ND with $\{111\}\langle 110 \rangle - \{111\}\langle 112 \rangle$
 η fibre
 $\langle 001 \rangle \parallel$ RD with $\{001\}\langle 100 \rangle - \{011\}\langle 100 \rangle$ (Goss)
 ζ fibre
 $\langle 110 \rangle \parallel$ ND with Goss, $\{110\}\langle 112 \rangle$ and $\{110\}\langle 110 \rangle$
 ϵ fibre
 $\langle 110 \rangle \parallel$ TD with $\{001\}\langle 110 \rangle$, $\{112\}\langle 111 \rangle$, $\{4\ 4\ 11\}\langle 11\ 11\ 8 \rangle$,
 $\{111\}\langle 112 \rangle$, $\{11\ 11\ 8\}\langle 4\ 4\ 11 \rangle$ and $\{011\}\langle 100 \rangle$ (Goss)
 β fibre
 $\{111\} \parallel$ ND, $\{111\}\langle 110 \rangle$, $\{111\}\langle 112 \rangle$, $\{557\}\langle 583 \rangle$, no static fibre,
 ϕ_1 is abscissa, ϕ_2 and Φ can vary according to maximum
RD, ND, and TD are rolling, normal, and transverse directions,
respectively

Table 1 Chemical compositions of alloys under investigation (balance Fe), wt-%

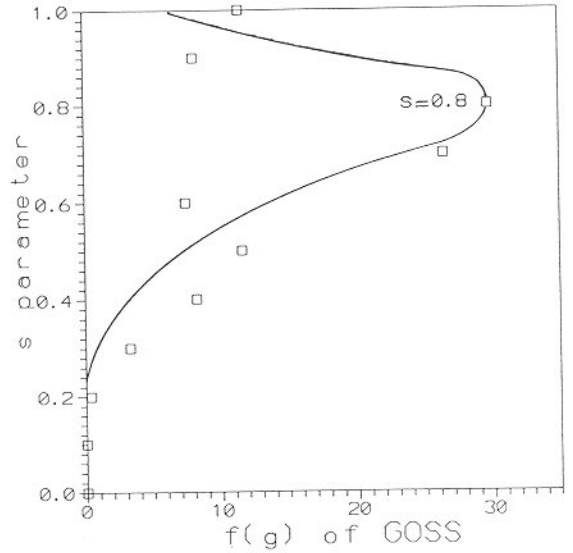
Sample code	C	Cr	N	Nb	Ti
CR11TI	0.01	11.3	0.01	...	0.21
CR11NB	0.01	10.5	0.02	0.32	0.11
CR17	0.06	16.5	0.03	0.01	0.01
CR17TI	0.02	16.5	0.01	0.01	0.47
CR17NB	0.02	16.6	0.02	0.64	0.01



a, c centre texture ($s=0$) with strong α fibre; *b, d* subsurface texture ($s=0.8$) with strong $\{011\}\langle 100 \rangle$ component (Goss)
 2 Hot rolling texture with {110} pole figure and ODF in ϕ_1 sections for *a, b* sample CR11NB and *c, d* sample CR17NB

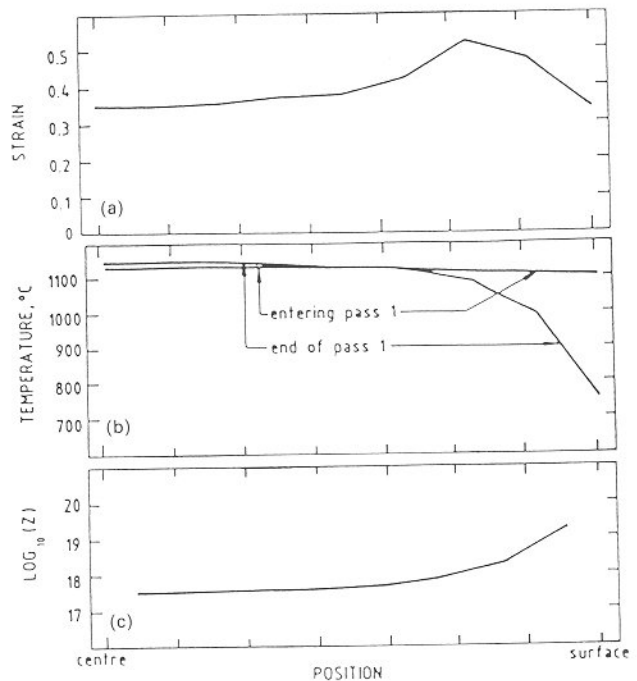


3 Fibre diagrams of hot rolling texture in through thickness steps $\Delta s=0.1$ for CR17NB

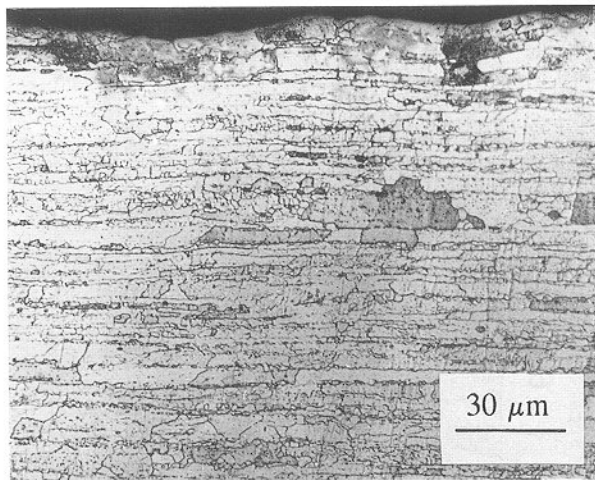


4 Profile of $\{011\}\langle 100 \rangle$ component (Goss) through thickness of CR17NB hot band: $s=0$ at centre and $s=1.0$ at surface

Since the texture and microstructure of ferritic steels is very inhomogeneous through the thickness, for all samples measurements were taken at four different depths. The hot rolled material, from where this inhomogeneity proceeds, has even been measured at eleven different depths. The actual layer is described by the parameter s , which represents the distance between layer and sample centre divided by the half thickness ($s=0$ centre, $s=1$ surface). To remove a surface layer of $20\text{ }\mu\text{m}$ for texture measurements, the samples containing 11%Cr were etched in a solution of 50 ml H_2O_2 and 10 ml HF, whereas those containing 17%Cr were etched in a solution of 100 ml H_2O_2 , 10 ml HF, 5 ml HNO_3 , and 5 ml HCl. Metallography was carried out applying scanning electron and optical microscopy to reveal the inhomogeneity of the microstructure through the thickness of the hot bands and to measure the size and distribution of the particles.



5 Calculated through thickness profiles of a strain,¹⁴ b temperature,¹⁴ and c Zener-Hollomon parameter¹⁴



6 Optical micrograph of sample CR17 taken in longitudinal direction

Results and discussion

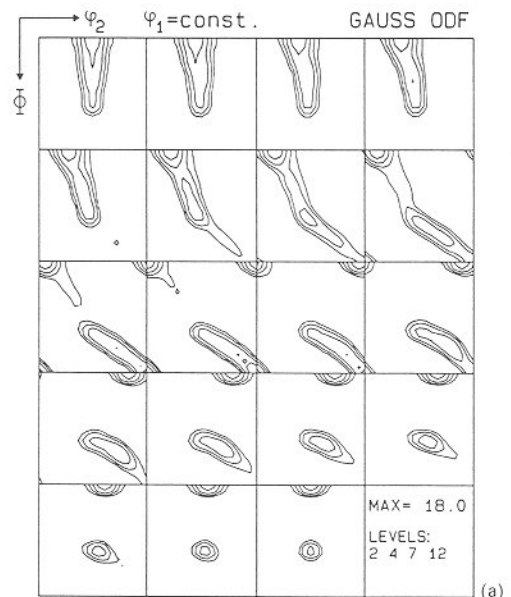
HOT ROLLING

Owing to their high Cr and low C contents the 17%Cr alloyed steels do not undergo phase transformation during hot rolling. The 11%Cr alloyed steels reveal up to 20 vol.-% phase transformation during the first steps of hot rolling.⁸ In Figs. 2a, b and 2c, d the hot rolling textures of samples CR11NB and CR17NB, respectively are presented by means of $\{110\}$ pole figures and ODFs from two layers. Whereas close to the surface ($s=0.8$) a strong $\{011\}\langle 100 \rangle$ component (Goss) is developed, in the central layer ($s=0$) a strong α fibre is revealed. For both layers the 17%Cr sample reveals a sharper texture.

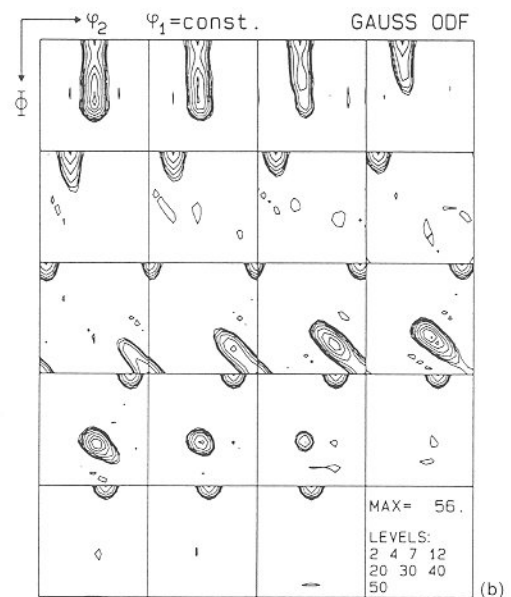
In Fig. 3 the texture is presented in through thickness steps $\Delta s=0.1$ for sample CR17NB in fibre diagrams. At the centre ($s=0$) the texture is dominated by a sharp α fibre (Fig. 3a), whereas close to the surface ($s=0.7-1.0$) the texture is characterised by the orientations $\{011\}\langle 100 \rangle$ (Goss), $\{4411\}\langle 11118 \rangle$ (Fig. 3b) and $\{110\}\langle 112 \rangle$ (Fig. 3c). This texture profile through the thickness is also known from Fe-3Si hot band,^{7,9,10} thermomechanically hot rolled low carbon steel,¹¹ and torsion experiments.¹²

In Fig. 4 the profile of the Goss component through the thickness of CR17NB reveals a maximum between $s=0.7$ and 0.9 . This typical Fe-Cr subsurface texture ($s=0.8$) results from strong shear deformation.^{7,10,13} The intensities of the shear components $\{011\}\langle 100 \rangle$ (Goss), $\{110\}\langle 112 \rangle$, and $\{4411\}\langle 11118 \rangle$ correspond to the profile of strain (Fig. 5a), resulting from the influence of the temperature curve (Fig. 5b) on the flow stress and the through thickness profile of the Zener-Hollomon parameter (Fig. 5c), as estimated by Beynon *et al.*¹⁴ These shear conditions are continuously weakened through the thickness so that the centre of the sheet is finally deformed by plain strain.

As mentioned above, the temperature profile through the sheet thickness must be taken into account (Fig. 5b).¹⁴ The water spray just in front of each rolling gap reduces the surface temperature of the sheet. This leads to a higher stored dislocation energy and thus to some recrystallised grains close to the surface. In the central layer the temperature remains high enough for dynamic recovery, which prevents nucleation and primary recrystallisation. The resulting microstructure having 'pancake' morphology and some equiaxed grains at the surface is revealed in Fig. 6.^{7,10} It must be emphasised that the differences between surface and centre are much smaller in the microstructure than in the texture.



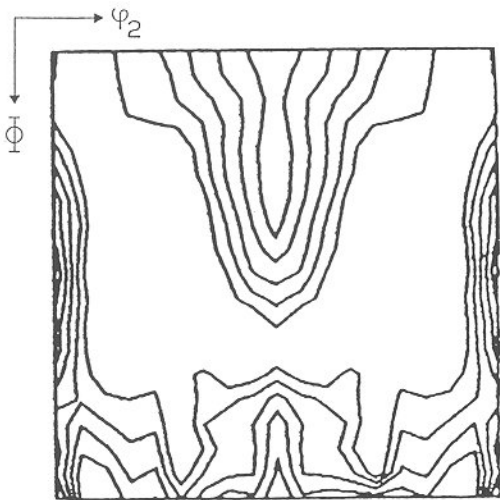
TAYLOR RC $\epsilon_{13}+\epsilon_{23}$, 110, 112, 123



TAYLOR RC $\epsilon_{13}+\epsilon_{23}$, 110, 112, 123

7 Taylor relaxed constraints simulation for a 60% and 99.9% deformation with relaxed ϵ_{13} and ϵ_{23} shear from initial random texture: activation of $\{110\}\langle 111 \rangle$, $\{112\}\langle 111 \rangle$, and $\{123\}\langle 111 \rangle$ glide systems

The combination of recovery, plane strain deformation, and flat grain morphology leads to a typical 'cold rolling' texture at the centre of the hot band, which can be simulated by means of the relaxed constraints Taylor theory.¹⁵ These simulations are based on the description of macroscopic deformation by means of crystallographic slip. Macroscopic deformation is described by the displacement gradient tensor. The symmetric part represents the strain tensor, while the antisymmetric part represents the resulting rigid body rotation. Rolling deformation consists of thickness reduction parallel to the sheet normal and elongation in the rolling direction. The relaxed constraints Taylor theory assumes also shear strains to occur microscopically between adjacent grains. A relaxation of the ϵ_{13} strain component corresponds to longitudinal shear and of ϵ_{23} to transverse shear. Allowing for these shear strain components to occur microscopically leads to distinct changes in the texture. The textures presented in Figs. 7a and 7b were calculated with relaxed ϵ_{13} and ϵ_{23} shear, due to the flat

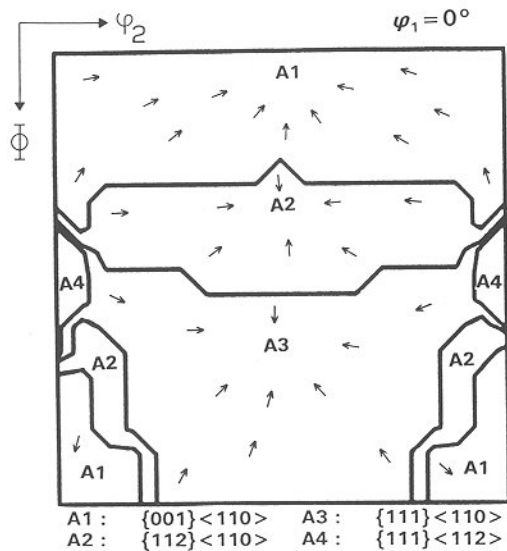


8 $\varphi_1 = 0^\circ$ section in reduced Euler space with isovelocity lines for rotations of crystals: strong minima for α fibre ($\varphi_2 = 45^\circ$) and for Goss ($\Phi = 45^\circ$)

and elongated grain morphology in the centre (Figs. 2a and 2c). In this simulation the $\{110\}\langle 111\rangle$, $\{112\}\langle 111\rangle$, and $\{123\}\langle 111\rangle$ glide systems were taken into account, according to the high deformation temperature during hot rolling.

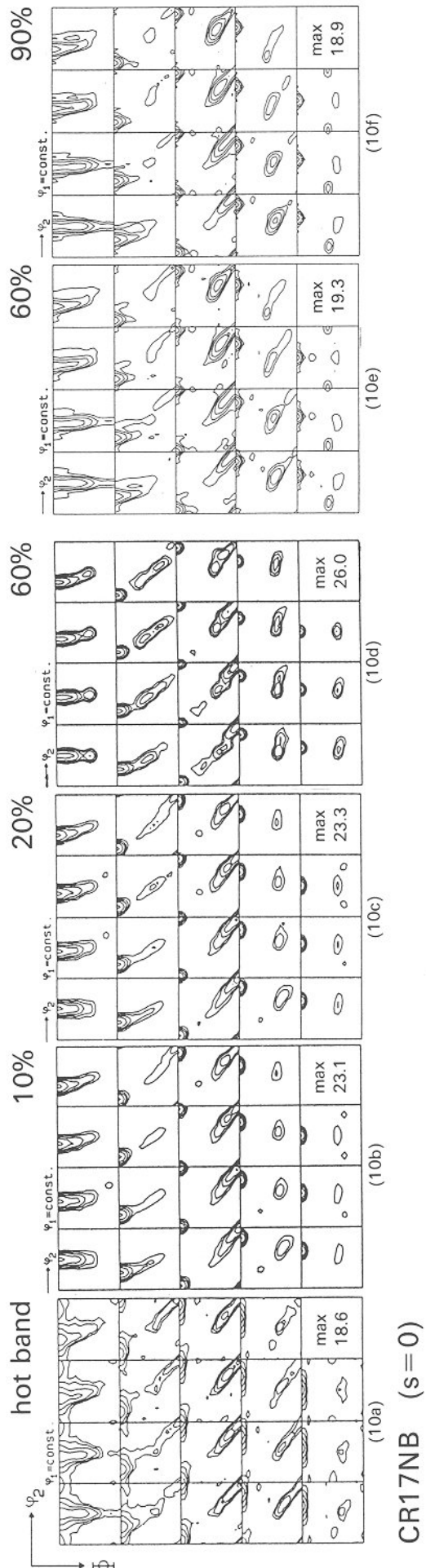
The strong α fibre texture at the centre of the hot bands also causes roping, especially in Fe-17Cr.^{16,17} The main components $\{112\}\langle 110\rangle$ and $\{111\}\langle 110\rangle$ both deform by asymmetric activation of glide systems, leading to ε_{23} shear. Any statistical topological arrangement of these components in the elongated hot band morphology leads to the observed macroscopic roping.¹⁶ Only a reduction of these components in the hot band texture, a change of the deformation mode, or the randomisation of the texture by phase transformation could therefore prevent roping.

The strong component at $\Phi = 0^\circ$ close to the rotated cube $\{001\}\langle 110\rangle$ is assumed to stem from a fibre with $\{001\}$ parallel normal direction, which is known for high growth rates during continuous casting.^{18,19} Although all the alloys investigated reveal the same through thickness texture profile, the hot band texture of steels containing 11%Cr is weaker than that of those containing 17%Cr. This is due to the randomisation of the rolling texture of 11%Cr samples because of phase transformation during the first hot rolling passes.

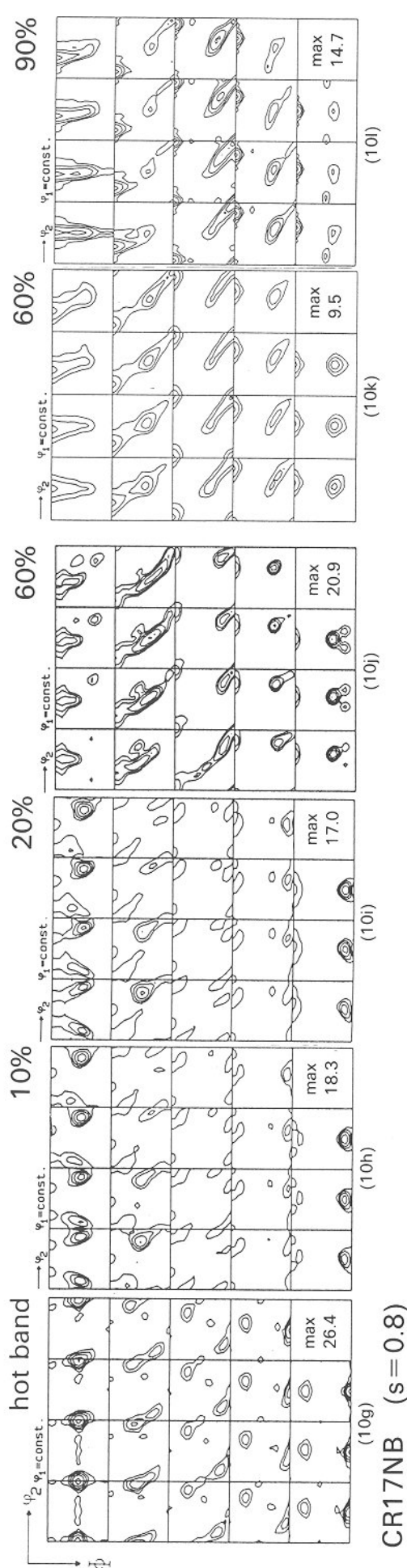


A1 : $\{001\}\langle 110\rangle$ A3 : $\{111\}\langle 110\rangle$
A2 : $\{112\}\langle 110\rangle$ A4 : $\{111\}\langle 112\rangle$

9 $\varphi_1 = 0^\circ$ section in reduced Euler space with catchment areas of four deformational attractors A1-A4

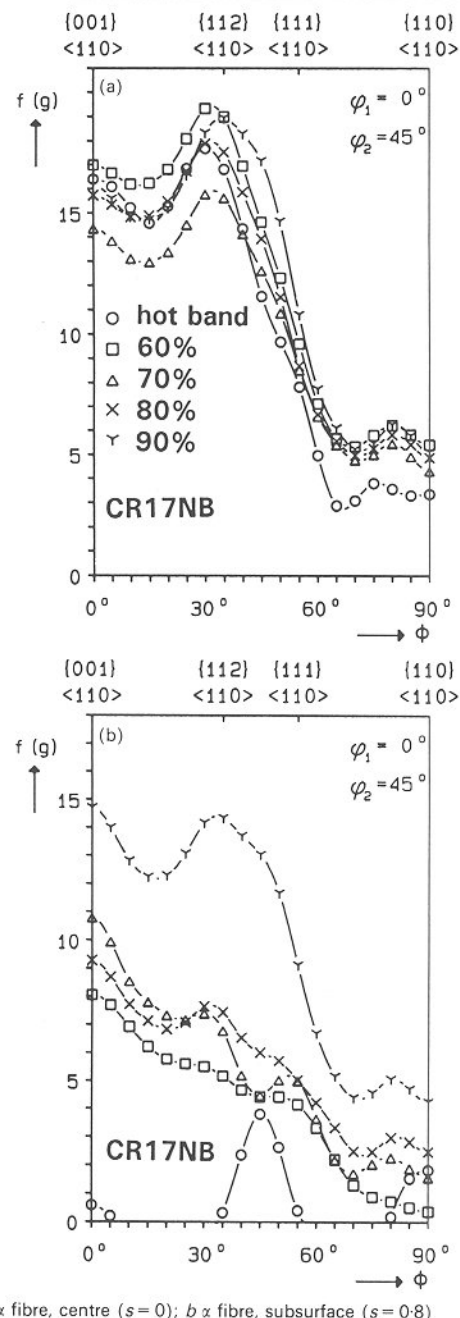


CR17NB ($s=0$)



Taylor simulations with initial hot band texture for *a*, *g* initial hot band; *b*, *h* 10% simulated cold rolling (SCR); *c*, *i* 20% SCR; and *d*, *j* 60% SCR. Measured texture after *e*, *k* 60% CR and *f*, *l* 90% CR

10 Simulated and measured ODFs for sample CR17NB at *a*-*f* centre (*s*=0) with relaxed ϵ_{13} and ϵ_{23} shear strain components and *g*-/*subsurface* (*s*=0.8) with relaxed ϵ_{13} shear strain component

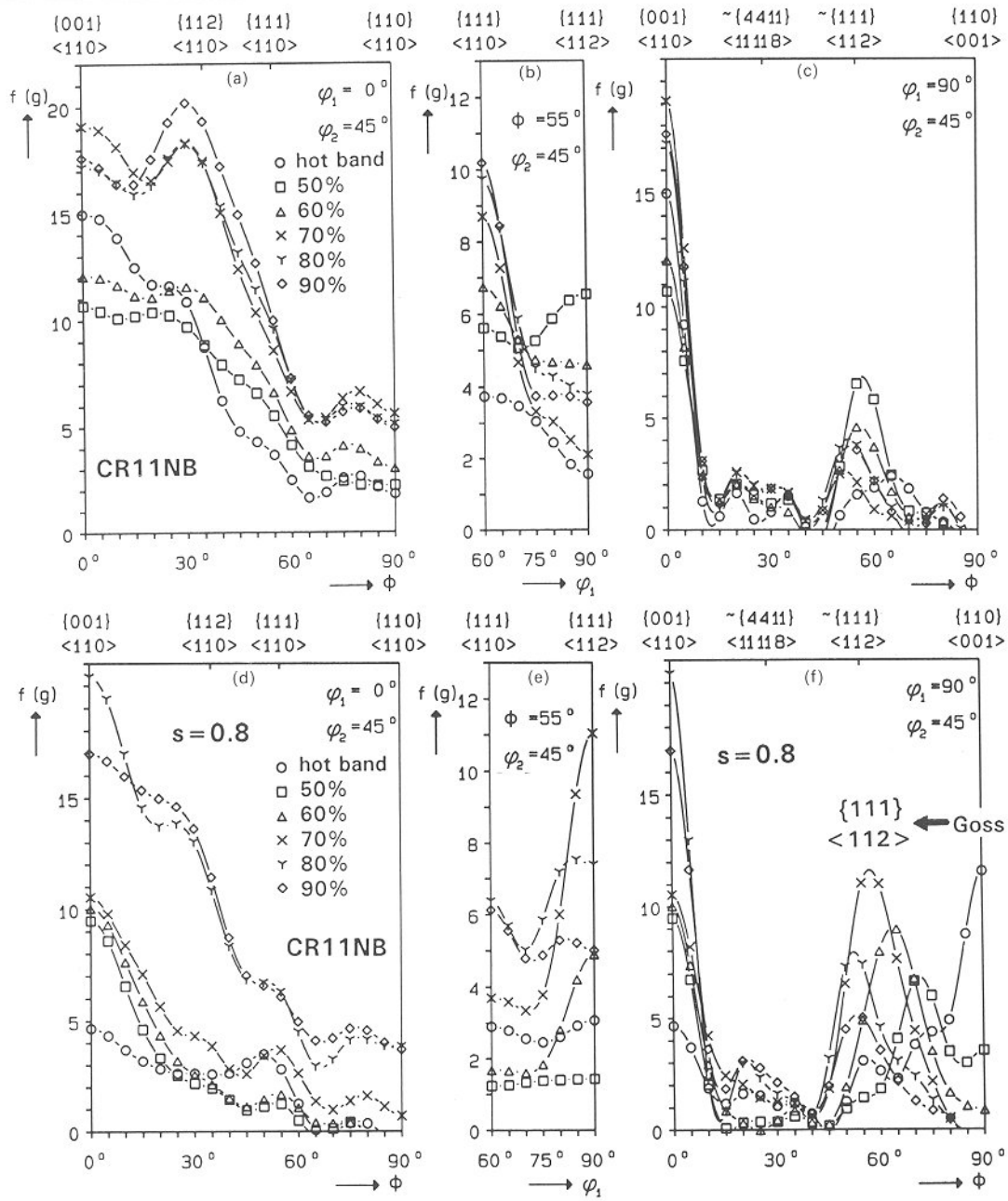


11 Fibre diagrams of development of cold rolling texture for CR17NB

COLD ROLLING

By means of Taylor simulations, two main features of cold rolling textures, except prediction of stable end orientations, can be calculated, namely, the velocity of rotation and the catchment areas of 'deformational attractors'. Typical stable orientations according to Taylor simulation with relaxed ϵ_{13} and ϵ_{23} constraints are shown in Fig. 7. In Fig. 8 the calculated rotational velocities, admitting slip on {110}, {112}, and {123} planes, are presented in the $\phi_1 = 0^\circ$ section. The result is that all orientations on the α fibre reveal very slow rotation rates, although they do not all represent typical stable end orientations. Hence, all orientations, once rotated into this α fibre, will become metastable.

The Goss orientation is a very labile orientation. Although it reveals a low rotational velocity (Fig. 8), already smallest deviations of the ideal orientation will lead to a rotation towards {001}<110> on the α fibre or {111}<112> on the γ fibre. These contrary rotations of two



a, d α fibre; b, e γ fibre; c, f ϵ fibre

12 Fibre diagrams of development of cold rolling texture at a-c centre and d-f subsurface of CR11NB

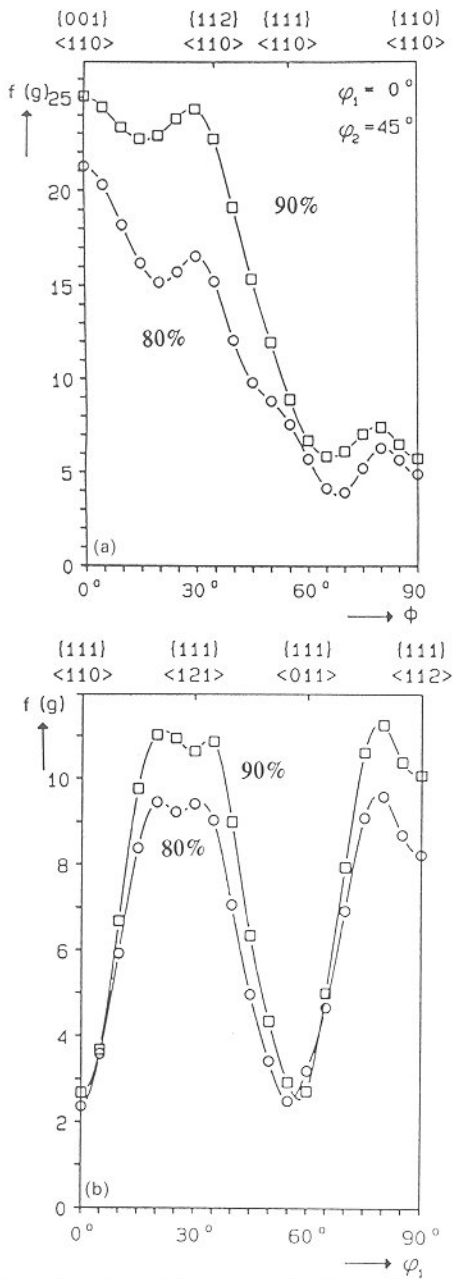
parts within one initial Goss grain can lead to the formation of transition bands.²⁰

The question of rotational directions illustrates the meaning of catchment areas surrounding stable orientations in Euler space. Stable orientations can be interpreted as deformational attractors, because they 'collect' non-stable orientations and force them to rotate into a stable one. Therefore, it is important to know the location and size of the catchment area of a stable orientation, because it defines the potential intensity of this orientation after cold rolling. For a random orientation distribution with $f(g) = 1$, the potential of a deformational attractor is identical with the $f(g)$ value of the stable end orientation. However, small deviations with $f(g) > 1$ in the initial catchment field will considerably change the intensity of the stable end orientation. In Fig. 9, the calculated attractors and their catchment areas in the $\phi_1 = 0^\circ$ section are shown for relaxation of ϵ_{23} shear. It is also expected that the competition of several catchment fields in the vicinity of certain orientations, e.g. Goss (Fig. 9), favours the formation

of transition bands, because several parts of the initial grain may rotate into various directions.

Taylor simulations therefore can be used to investigate: the origin of an orientation (Fig. 9, catchment area), to where it rotates (Fig. 7, stable end orientation), and at what rate (Fig. 8, velocity of rotation). It can be inferred from this that the development of cold rolling textures is strongly dependent on the initial hot rolling textures.^{7,10}

According to different grain shapes and initial textures, the development of the cold rolling texture was calculated at the centre ($s = 0$) with relaxed ϵ_{13} and ϵ_{23} shear strain components and at the subsurface ($s = 0.8$) with relaxed ϵ_{13} for sample CR17NB (Figs. 10a-d and 10g-j). For this purpose the original ODFs (Figs. 10a and 10g) were fitted with 1000 orientations. The experimental ODFs (Figs. 10e, f and 10k, l) correspond very well with the simulations. It can be seen that the Goss component at $s = 0.8$ rotates rapidly to $\{111\}\langle 112 \rangle$ (Figs. 10j, 10k). The α fibre at the centre is much sharper than at the surface owing to the stronger initial α texture (Figs. 10d and 10e). After 90%



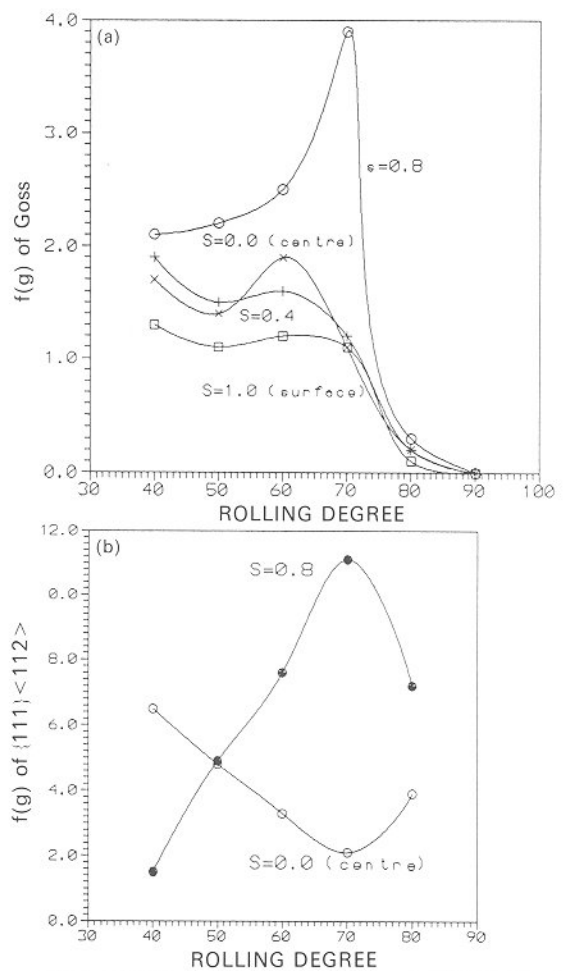
a α fibre, cold rolled; b β fibre, recrystallised (max. density)

13 Rolling and recrystallisation texture at centre of sample CR17

rolling the textures have become very similar in both layers (Figs. 10f and 10l). In the fibre diagrams (Fig. 11) it can be seen that the texture in the central layer of CR17NB remains almost constant during cold rolling, because all stable orientations are already present after hot rolling.

Materials CR11NB and CR11TI reveal very similar behaviour during cold rolling. On the α fibre the centre reveals the strongest rolling components $\{001\}\langle 110 \rangle$ – $\{112\}\langle 110 \rangle$ (Fig. 12a), whereas at the subsurface ($s=0.8$) the α fibre develops much more slowly, owing to the initial shear texture (Fig. 12d). On the ε fibre (Fig. 12f) the rotation of Goss into $\{111\}\langle 112 \rangle$ is presented, leading to a strong maximum on the γ fibre (Fig. 12e) at the subsurface layer after 70% deformation. This $\{111\}\langle 112 \rangle$ maximum is important for nucleation of Goss during primary recrystallisation.

The variation of the Nb and Ti content did not lead to distinct changes in the cold rolling textures. Concerning the Cr content, differences can be seen for the location of



a Goss component after recrystallisation; b $\{111\}\langle 112 \rangle$ after cold rolling

14 Intensity of texture in CR11NB for various degrees of rolling and at various layers

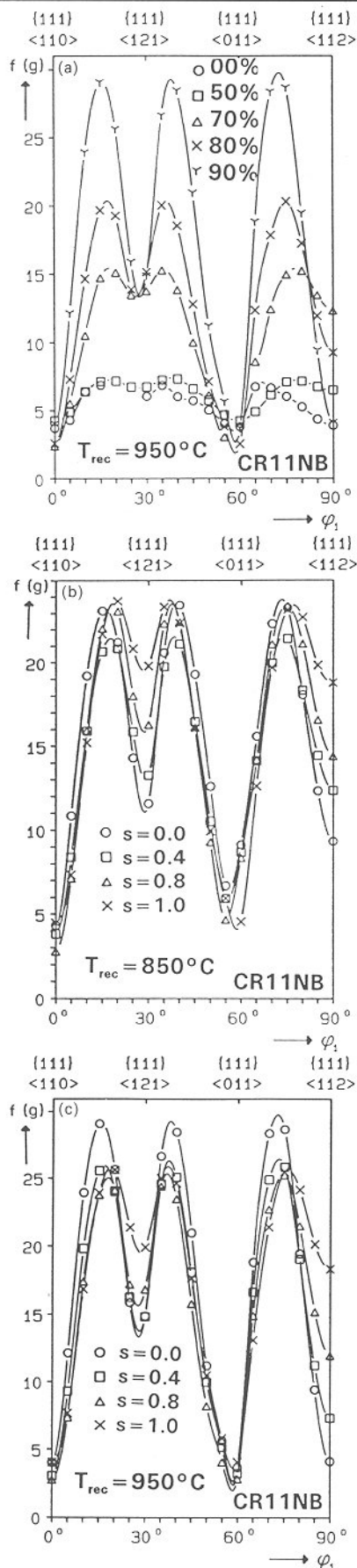
$\{112\}\langle 110 \rangle$, which is shifted from $\Phi = 35^\circ$ for the 17%Cr alloyed steels to $\Phi = 30^\circ$ for the 11%Cr alloyed steels. Moreover, the surface textures of the 11%Cr alloys reveal a slower sharpening of the α fibre than the 17%Cr alloys, so that also after 90% rolling there is still a strong texture gradient through the thickness.

ANNEALING

The annealing textures depend on the initial cold rolling texture and microstructure. In Fig. 13 the rolling and recrystallisation textures are shown for sample CR17. The maximum at $\{111\}\langle 112 \rangle$ after primary recrystallisation, well known for bcc steels,^{3–7} can be interpreted by the $35^\circ \langle 110 \rangle$ rotational relationship between $\{111\}\langle 112 \rangle$ and the strong rolling component $\{112\}\langle 110 \rangle$. This relationship is close to the ideal $27^\circ \langle 110 \rangle$ rotation, characterised by a $\Sigma 19a$ coincidence (Σ is the reciprocal of the density of coinciding sites). Owing to the high mobility of this special boundary the $\{111\}\langle 112 \rangle$ nuclei can selectively grow into the $\{112\}\langle 110 \rangle$ matrix.²¹

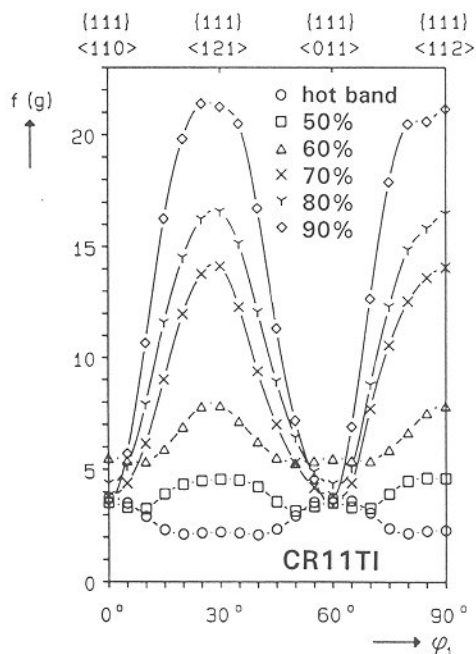
In bicrystal experiments, it was shown for Fe (Ref. 22) that $\{111\}\langle 112 \rangle$ may also develop from oriented nucleation close to former grain boundaries in $\{111\}\langle 110 \rangle$, which yields the highest dislocation densities²³ and the highest nucleation rates.²⁴ In correspondence with the weak $\{111\}\langle 110 \rangle$ intensity in the deformation matrix, however, growth selection is supposed to represent the leading mechanism in the formation of $\{111\}\langle 112 \rangle$.

After 50–70% rolling, the increase of the Goss component can also be seen in the annealing texture (Fig. 14a). The



a $T_{\text{rec}} = 950^\circ\text{C}$, centre texture for various degrees of rolling; b $T_{\text{rec}} = 850^\circ\text{C}$ after 90% cold rolling for various layers; c $T_{\text{rec}} = 950^\circ\text{C}$ after 90% cold rolling for various layers

15 Recrystallisation texture of CR11NB with strong maxima at $\sim\{557\}\langle 583 \rangle$ in β fibre presentation: annealing time 5 min



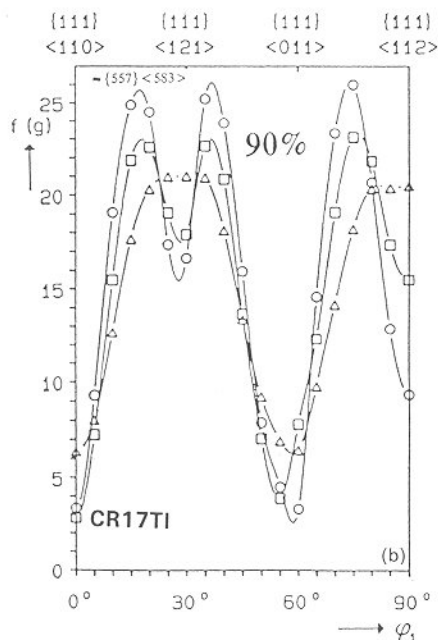
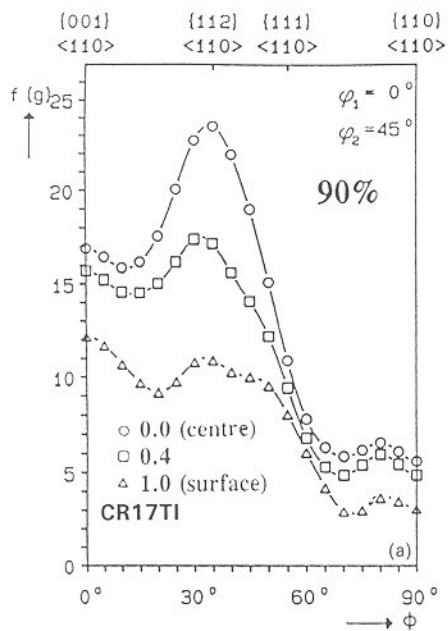
16 Rolling and recrystallisation texture of CR11TI with strong maxima at $\{111\}\langle 112 \rangle$ in β fibre presentation: $T_{\text{rec}} = 950^\circ\text{C}$, 5 min

maximum of the Goss after 70% deformation and annealing correlates with the maximum of $\{111\}\langle 112 \rangle$ in the rolling texture (Fig. 14b) at $s=0.8$. In this layer, the Goss component was inherited from the hot rolled material and rotated during cold rolling under plain strain deformation towards $\{111\}\langle 112 \rangle$ and $\{001\}\langle 110 \rangle$, respectively (Figs. 10g–j, 12f). These divergent rotations supposedly led to the maintenance of transition bands with preserved Goss orientation between the rotated fragments. Owing to the fine cell structure and high local misorientations, it is thus expected that Goss may nucleate in the transition bands.²⁰

In previous works, especially on Fe–3Si textures, the correlation between $\{111\}\langle 112 \rangle$ in the rolling texture and Goss in the annealing texture was explained by nucleation of Goss in shear bands.^{25–27} However, in the present alloys, only very weak shear banding occurs, due to the small grain size and the interstitial free matrix, so that nucleation in transition zones is considered to represent the main mechanism of Goss formation in Fe–Cr.

In addition to the formation of $\{111\}\langle 112 \rangle$ and $\{011\}\langle 100 \rangle$ in Fe–Cr alloys, the recrystallisation of samples with stable particles can lead to a new component $\sim\{557\}\langle 583 \rangle$ instead of the classical $\{111\}\langle 112 \rangle$ maximum.²⁸ In Fig. 15a, the increase of $\{557\}\langle 583 \rangle$ is presented for recrystallisation of CR11NB at 950°C . The maximum is shifted $\sim 10^\circ$ from $\{111\}\langle 112 \rangle$ and increases with degree of rolling. It can be seen in Figs. 15b and 15c that $\{557\}\langle 583 \rangle$ increases for all layers with higher annealing temperature. The measurements present a good correlation between the intensity of $\{112\}\langle 110 \rangle$ in the rolling texture (Figs. 12a–12c) and $\{557\}\langle 583 \rangle$ in the annealing texture. The exact positions of both orientations reveal an ideal $27^\circ\langle 110 \rangle$ rotational relationship. However, the recrystallisation texture of CR11TI shows a classical maximum at $\{111\}\langle 112 \rangle$ (Fig. 16), whereas sample CR17TI reveals the same maximum as CR11NB at $\{557\}\langle 583 \rangle$ (Fig. 17).

The development of this component can be explained by selective particle drag.²⁸ The Ti and Nb carbonitrides are precipitated before hot rolling and hence are randomly distributed in the microstructure without necessarily being connected to subboundaries or high angle grain boundaries. In this case, the formula for particle drag can be written as



a α fibre, cold rolled; b β fibre, recrystallised (max. density)

17 Rolling and recrystallisation texture of sample CR17Ti in various layers

$F_p = (6\gamma f)/(\pi R)$, where F_p is the particle drag force, γ is the grain boundary energy, f is the precipitated volume fraction of particles, and R is the average particle radius.

The particle drag forces calculated for CR11NB, CR11Ti, CR17NB, and CR17Ti for coincident (F_p^{\min}) and non-special (F_p^{\max}) grain boundaries are presented in Table 2. Owing to the duplex system of Nb and Ti carbonitrides in fine precipitation, sample CR11NB yields the highest drag forces of 21.6 kN m^{-2} , whereas CR11Ti reaches only 6.2 kN m^{-2} . The driving forces for primary recrystallisation of Fe–Cr steels are of the magnitude $F_r \approx 10^2 \text{ kN m}^{-2}$, because the precipitations extend the incubation period, so that strong recovery can take place. Hence, the driving forces for recrystallisation are of the same magnitude as the particle drag forces for non-special grain boundaries in CR11NB, CR17NB, and CR17Ti (F_p^{\max} in Table 2). Because the drag forces are proportional to the grain boundary energy, coincident boundaries are not hindered by particles ($F_p^{\min} = F_p^{\text{coincident}} \ll F_r$, Table 2). Therefore, this mechanism

Table 2 Particle drag forces in samples of microalloyed steels

Sample*	$R, \mu\text{m}$	$f/10^{-3}$	$F_p^{\min}, \text{kN m}^{-2}$	$F_p^{\max}, \text{kN m}^{-2}$
(CR11NB) _{Nb}	0.25	3.30	$F_p^{\min} = F_p^{\min} + F_p^{\min}$	$F_p^{\max} = F_p^{\max} + F_p^{\max}$
(CR11NB) _{Ti}	0.20	1.13	$= 3.6$	$= 21.6$
CR17Ti	0.40	4.82	2.3	13.8
CR17NB	0.40	6.57	2.1	12.6
CR11Ti	0.40	2.16	1.0	6.2

*On CR11NB, subscripts Nb and Ti denote that only forces due to Nb and Ti particles respectively are considered.

R average particle radius; f precipitated volume fraction of microcarbid; F_p^{\min} drag force for coincident boundary; F_p^{\max} drag force for non-special boundary.

is termed grain boundary energy selective particle drag. For CR11Ti, the particle drag forces were too weak to have any influence on growth selection (Table 2). For fine dispersion, the retarding force of the particles is thus responsible for a strong growth selection during recrystallisation, which leads to the growth of $\{557\}\langle 583 \rangle$ nuclei into the $\{112\}\langle 110 \rangle$ deformation matrix because of their $27^\circ \langle 110 \rangle$ coincidence relationship.

Conclusions

1. Fe–Cr hot bands reveal shear texture with Goss texture at the surface and cold rolling texture with α fibre in the central layer.
2. Cold rolling leads to a strong α fibre texture in all layers with a maximum in the centre.
3. Increase of Cr content shifts $\{112\}\langle 110 \rangle$ to higher Φ angles on the α fibre.
4. Cold rolling textures can be simulated by means of models derived from relaxed constraints Taylor theory with relaxation of ε_{13} and ε_{23} .
5. Recrystallisation of 50–70% cold rolled samples with strong $\{111\}\langle 112 \rangle$ leads to Goss texture especially in the subsurface.
6. The development of Goss texture during annealing is dependent on the existence of transition bands.
7. Recrystallisation of cold rolled samples ($\varepsilon > 70\%$) without stable particles or with low dispersion rates leads to formation of $\{111\}\langle 112 \rangle$ by growth selection.
8. The presence of finely dispersed stable microcarbides can influence the recrystallisation texture by selective particle drag.

References

1. L. G. SCHULZ: *J. Appl. Phys.*, 1949, **20**, 1030.
2. H. J. BUNGE: 'Mathematical methods of texture analysis', 1969, Berlin, Akademie Verlag.
3. G. WASSERMANN and J. GREWEN: 'Texturen metallischer Werkstoffe', 1962, Berlin, Springer-Verlag.
4. U. v. SCHLIPPENBACH, F. EMREN, and K. LÜCKE: *Acta Metall.*, 1986, **34**, 1289.
5. C. DÄRMANN, M. HÖLSCHER, S. MISHRA, and K. LÜCKE: in Proc. 7th Int. Conf. on 'Texture of Materials' (ICOTOM 7), (ed. C.M. Brakman *et al.*), 759; 1984, Zwijndrecht, Netherlands Society for Materials Science.
6. S. MISHRA, C. DÄRMANN, and K. LÜCKE: *Acta Metall.*, 1984, **32**, 2185.
7. M. HÖLSCHER, D. RAABE, and K. LÜCKE: *Steel Res.*, 1991, **62**, (12), 567.
8. H. OUDREMONT: 'Handbuch der Sonderstahlkunde', 3 edn 1956, Berlin, Springer-Verlag.
9. L. SEIDEL, M. HÖLSCHER, and K. LÜCKE: *Textures Microstruct.*, 1989, **11**, 171.

10. D. RAABE and K. LÜCKE: *Scr. Metall.*, 1992, **26**, (8), 1221.
11. C. DÄRMANN: in Proc. 9th Int. Conf. on 'Texture of Materials' (ICOTOM 9), (ed. H. J. Bunge), 813; 1990, Paris, Société Française de Metallurgie.
12. W. A. BACKOFEN and B. B. HUNDY: *Trans. AIME*, 1953, **197**, 51.
13. T. J. RICKERT, J. A. SALSGIVER, and S. D. WASHKO: in Proc. Int. Conf. on 'Stainless Steels', 877-884; 1991, Tokyo, The Iron and Steel Institute of Japan.
14. J. H. BEYNON, A. R. S. PONTER, and C. M. SELLARS: in Proc. Conf. 'Modelling of metal forming', 321; 1988, London, Kluwer Academic.
15. H. HONNEFF and H. MECKING: in Proc. 5th Int. Conf. on 'Texture of Materials' (ICOTOM 5), (ed. G. Gottstein and K. Lücke), 457; 1978, Aachen, RWTH.
16. M. HÖLSCHER: PhD thesis, RWTH Aachen, 1987.
17. H. TAKECHI, H. KATO, T. SUNAMI, and T. NAKAYAMA: *Trans. Jpn Inst. Met.*, 1967, **8**, 233.
18. Y. SHIMIZU, Y. ITO, and Y. IIDA: *Metall. Trans.*, 1986, **17A**, 1323.
19. M. F. LITTMANN: *Metall. Trans.*, 1975, **6A**, 1041.
20. I. L. DILLAMORE, P. L. MORRIS, C. J. SMITH, and W. HUTCHINSON: *Proc. R. Soc.*, 1972, **A329**, 405-420.
21. G. IBE and K. LÜCKE: *Arch. Eisenhüttenwes.*, 1969, **39**, 33.
22. W. B. HUTCHINSON: *Acta Metall.*, 1989, **37**, (4), 1047.
23. I. L. DILLAMORE, C. J. E. SMITH, and T. W. WATSON: *Met. Sci.*, 1967, **1**, 49.
24. M. ABE, Y. YOKABU, Y. HAYASHI, and S. HAYAMI: *Trans. Jpn Inst. Met.*, 1982, **23**, 718.
25. K. USHIODA, H. OHSONE, and M. ABE: in Proc. 6th Int. Conf. on 'Texture of Materials', (ICOTOM 6) 829; 1981, Tokyo, The Iron and Steel Institute of Japan.
26. M. MATSUO: *ISIJ Int.*, 1989, **29**, (10), 809-827.
27. T. HARATANI, W. B. HUTCHINSON, I. L. DILLAMORE, and P. BATE: *Met. Sci.*, 1984, **18**, 57.
28. D. RAABE and K. LÜCKE: *Scr. Metall.*, 1992, **26**, 19.

FUTURE DEVELOPMENTS OF METALS AND CERAMICS



A collection of invited papers to mark the 70th birthday of Professor Sir Robert Honeycombe

Edited by J A Charles, G W Greenwood and G C Smith

This volume contains the invited papers presented at a meeting at the Royal Society in 1991 to honour Sir Robert Honeycombe's seventieth birthday and to mark his many contributions to materials science. Twelve papers cover the broad themes of materials' properties, processing and microstructure and assess the ways in which these areas are continuing to develop and are likely to move in the future.

Contents

- * Preface
- * Welcoming Comments
- * Advanced Light Alloys
- * High-Strength Steels
- * Microalloyed Steels
- * The Importance of Microstructural Characterisation in Improving Ceramics Engineering Applications
- * Thermomechanical Processing
- * Casting Technology
- * Powders and Direct Metal Processing
- * Welding Stainless Steels
- * Laser Surface Treatments
- * Electron Materialography
- * Metals and Ceramics - Mechanical Properties
- * Microstructural Refinement of Duplex Stainless Steels
- * Concluding Remarks
- * Professor Sir Robert Honeycombe: Published Works

Book 518 234x156mm 376pp (H) 0 901716 03 0 1992 £55.00 US\$110.00 (Students: £25.00 US\$50.00)

Orders with remittance* to: The Institute of Materials, Sales & Marketing Dept., 1 Carlton House Terrace, London SW1Y 5DB. Tel. 071-976 1338 Fax. 071-839 2078

Orders originating in Canada and the United States should be sent direct to: Ashgate Publishing Co., Old Post Road, Brookfield, VT 05036, USA. Tel (802) 276 3162 Fax. (802) 276 3837

*Carriage: UK customers please add £2.50 per order, overseas customers add US\$6.00